Spectroscopy of Ba^+ ions in liquid ^4He

R. Batulin, P. Moroshkin, D. A. Tayurskii, and K. Kono

Citation: AIP Advances **8**, 015328 (2018);
View online: https://doi.org/10.1063/1.5011447
View Table of Contents: http://aip.scitation.org/toc/adv/8/1
Published by the American Institute of Physics

Spectroscopy of Ba^+ ions in liquid ^4He

R. Batulin,[1,2,a] P. Moroshkin,[1] D. A. Tayurskii,[2] and K. Kono[1,2]
[1]*RIKEN CEMS, 2-1 Hirosawa, Wako, Saitama 351-0198, Japan*
[2]*Institute of Physics, Kazan Federal University, 18 Kremlyovskaya St., Kazan 420008, Russian Federation*

(Received 2 October 2015; accepted 21 January 2018; published online 29 January 2018)

Atomic ions and free electrons embedded in condensed helium play important role in modern research on quantum fluids and solids. Here we present experimental and theoretical study of Ba^+ cations immersed in superfluid He. We observe laser-induced fluorescence of Ba^+ injected into liquid He from the plasma of radio frequency discharge in He-Ba gas mixture. The structure of trapping site is studied theoretically in the frame of the atomic bubble model making use of *ab initio* Ba^+ - He pair potentials available in the literature. Calculated spectra of the ion are compared with the results of the experiment. https://doi.org/10.1063/1.5011447

I. INTRODUCTION

Together with free electrons and He^+ cations, Ba^+ ion is a model object to study the properties of charged impurities in superfluid helium. Historically, the first mobility measurements of Ba^+ in liquid He were reported back in 1972 by Johnson and Glaberson[1] and the first spectroscopic study was carried out by Reyher *et al.*[2] in 1986. It is well established since 1960-ies that free electrons in liquid He form cavity-like trapping sites, known as electron bubbles, whereas the positive He ions are surrounded by solid-like clusters of He, known as snowballs. However, much more debate has emerged[3–7] about the structure and properties of Ba^+ and other alkali-earth cations in liquid He.

The bubble state occurs due to Pauli principle repulsion between the free electron and the closed electron shells of surrounding helium atoms. In equilibrium this force is balanced by the surface tension and external hydrostatic pressure on the bubble interface and leads to a bubble radius of 17 Å. Many neutral impurities, in particular atoms of most metallic elements, form bubbles, that are similar to the electron bubble and have typical radii of some 5 to 7 Å. In this case the repulsive force acts between the electron shells of the He atoms and the valence electrons of the dopant (for a review on atomic bubbles see Ref. 8).

For the snowball, a local enhancement of liquid helium density around the dopant occurs because of the attractive polarization force that acts on He atoms in the strongly inhomogeneous electric field of the ion. It was first predicted by electrostriction theory[9] that this increase in the local He density around He^+ results in solidification of liquid He and formation of a solid snowball with a radius of 8 Å. Alkali-metal cations also have a snowball-like structure either in bulk liquid helium[10] or in helium nanodroplets.[11]

Single-charged cations of alkali-earth elements, such as Ba^+ represent a more complicated system that falls in between the two limiting cases of a bubble and a snowball. Their electronic structure is equivalent to that of a neutral alkali-metal atom with a single valence electron occupying a spherically symmetric $n^2S_{1/2}$ (n=6 for Ba^+) orbital with electron density extending over several angstroms. The repulsive interaction between this electron and the closed electron shell of He atom dominates the Ba^+ - He interaction at interatomic distances below 5 Å. On the other hand, the electric field created by the ion makes the approaching He atom polarized and results in the attractive force that dominates over

[a]Electronic mail: tokamak@yandex.ru

the Pauli repulsion at distances larger than 5 Å. The resulting trapping site structure is determined by the interplay of these two mechanisms and may combine the features of the bubble and the snowball.

The time of flight measurements[1,3,12,13] have shown that the alkali-earth cations, including Ba^+, in superfluid He have slightly higher mobilities than the much lighter He^+ ions in disagreement with the standard snowball model. It was then suggested by Cole and Bachman[4] that the trapping site may be better visualized as an atomic bubble with a radius of 4-5 Å surrounded by compressed, but not solidified, helium. Mobilities of Ba^+ and several other positive and negative atomic ions were investigated in a recent theoretical work,[6] where the structure of the He complex around the ion is computed using time-dependent density-functional theory (DFT). The resulting He density profile resembles a bubble with a radius of ≈ 4.5 Å, surrounded by a pronounced high-density shell structure. The total radius of the defect is estimated as 11.6 Å.

Optical spectra of impurities in liquid He are particularly sensitive to the details of the trapping site structure and of the dopant-helium interaction. Spectroscopic studies of impurities in bulk superfluid helium, He films and He nanodroplets have attracted significant attention in the past 20 years and were reviewed in Refs. 8 and 14. Absorption and emission spectra of the two strongest electronic transitions of Ba^+ in bulk liquid He were observed by the Heidelberg group[2] in 1986. It was concluded that Ba^+ resides in a bubble-like trapping site. The atomic bubble calculations were developed later[5] to model the observed excitation spectra. The calculations significantly underestimated the observed line shift. The discrepancy was attributed to the imprecision in the calculated Ba^+-He interaction energy.

More recently, the spectroscopic study of Ba^+ attached to He nanodroplets was reported.[15] The observed excitation spectra are identical to those observed earlier[2] in bulk liquid He indicating that the ion in its electronic ground state is trapped at the center of the nanodroplet. The observed absorption spectra, the process of ion solvation, and the dynamics of the photoexcited ion were modeled by time-dependent DFT calculations in Refs. 7 and 16. Ba^+ ion was predicted to be a sensitive probe to investigate exotic excitations at the surface of superfluid helium and experiments are now in progress[17] aiming at trapping Ba^+ ions under a free surface and laser spectroscopy of such two-dimensional samples.

We also mention spectroscopic studies addressing the interaction between Ba^+ ions and He atoms in the gas phase. The experiments[18,19] have been carried out in a dense He gas at very high pressure and temperature: T = 3300 K, p = 1100 bar and provided Lorentzian lineshapes characteristic for the impact-broadening by elastic binary atomic collisions. The studies[20–22] of Ba^+ ion in a cryogenic He gas at T = 1.6-30 K concentrated on the energetics and formation mechanism of $Ba^{+\,*}$-He quasimolecules (excimers).

The present paper is organized as follows. In Sec. II we develop the atomic bubble model (ABM) for Ba^+ and it's extension deformed bubble model (DBM). These models are used to calculate the absorption and emission spectra. In Sec. III we present our method of injection of the ions into superfluid He and the observed spectra of laser-induced fluorescence of Ba^+ in bulk liquid He. In Sec. IV we compare the observed and calculated spectra and discuss the applicability of the bubble model and its usefulness as a simplified model for this complex many-body system.

II. THEORY

We apply the atomic bubble model (ABM) with ab-initio calculated pair-potentials to calculate Ba^+ spectrum (D_1 transition) in liquid helium.

A. Potential energy curves and spin-orbit interaction

The interaction between Ba^+ and surrounding He atoms is described with the help of pair potential energy curves obtained by *ab-initio* quantum chemistry calculations. Initially, potential energy curves, V^{pair}, were calculated in Refs. 20 and 23 for 6s Σ, 6p Σ and 6p Π states of a Ba^+ - He pair using MOLPRO software package. The complete-active-space self-consistent field (CASSCF) was used as a calculation method for molecular orbitals and the Ba^+ -He pair potentials were obtained by internally-contracted multireference configuration-interaction (MRCI) calculations in the same way

as in Ref. 24 for a Yb^+ -He pair. The pair potential curve for the ground state of Ba^+ interacting with He has been also reported in Refs. 6 and 25. More recently, a complete set of Ba^+-He pair potentials was calculated in Refs. 7 and 26 at the CCSD(T) level of theory.

It is known that CCSD(T) method allows one to calculate the electron correlation energy more accurately than the MRCI. Thus for the $6s\ \Sigma$ state the binding energy or dissociation energy D_e of a Ba^+-He pair has increased from 12 K for the pair potential[20,23] to 20 K for the pair potential[7,26] while the bond length R_e, has decreased from 5.7 Å to 5.0 Å, respectively.

Available pair potentials, describing the interaction between the electronically excited Ba^+ ion and the ground-state of a He atom do not take into account the spin-orbit interaction. The Ba^+-He potential energy depends on the orientation of the excited Ba^+ valence electron's orbital momentum $L = 1$ with respect to the internuclear axis, which results in two potential curves corresponding to degenerate $6p\ \Pi$ state with projections $M_L = \pm 1$ and to $6p\ \Sigma$ state with projection $M_L = 0$. The fine structure splitting of these states due to the spin-orbit interaction was calculated separately using diatomics-in-molecules (DIM) method.

The total Hamiltonian of a Ba^+-He pair $\hat{H}_{6P}^{pair}$ is written as a sum of the interaction Hamiltonian $\hat{H}_{int}$ and the spin-orbit interaction, $\hat{H}_{SO} = \xi \mathbf{LS}$. $S = 1/2$ is the electron spin and M_S - it's projection on the quantization axis. $\hat{H}_{int}$ is diagonal in $|n, L, M_L, M_s>$ representation and it's eigenvalues are given by the *ab initio* pair potentials V_Π^{pair} and V_Σ^{pair}. The spin-orbit coupling term $\hat{H}_{SO}$ is treated in a semi-empirical way using a standard procedure.[20,27] $\xi = 2/3\Delta$ is a spin-orbit coupling constant, where $\Delta = 20\,261.561\ cm^{-1}$ is the energy splitting between $6p\ ^2P_{1/2}$ and $6p\ ^2P_{3/2}$ states of a free Ba^+ taken from Ref. 28. The spin-orbit matrix is diagonal in the $|n, L, J, M_J>$ representation, where J and M_J are the total electronic angular momentum and it's projection, respectively. It is thus necessary to transform $\hat{H}_{SO}$ to the $|n, L, M_L, M_s>$ representation.[29] The total Hamiltonian $\hat{H}_{6P}^{pair}$ in representation $|n, L, M_L, M_S>$ is a block-diagonal matrix consisting of two 3×3 blocks.

$$H_{6P}^{pair}(R) = \begin{Bmatrix} V_\Sigma^{pair}(R) & \frac{\sqrt{2}}{3}\Delta & 0 & 0 & 0 & 0 \\ \frac{\sqrt{2}}{3}\Delta & V_\Pi^{pair}(R) - \frac{1}{3}\Delta & 0 & 0 & 0 & 0 \\ 0 & 0 & V_\Pi^{pair}(R) + \frac{1}{3}\Delta & 0 & 0 & 0 \\ 0 & 0 & 0 & V_\Sigma^{pair}(R) & \frac{\sqrt{2}}{3}\Delta & 0 \\ 0 & 0 & 0 & \frac{\sqrt{2}}{3}\Delta & V_\Pi^{pair}(R) - \frac{1}{3}\Delta & 0 \\ 0 & 0 & 0 & 0 & 0 & V_\Pi^{pair}(R) + \frac{1}{3}\Delta \end{Bmatrix} \quad (1)$$

The eigenenergies of the pair Ba^+-He including spin-orbit interaction are obtained by diagonalization of H_{6P}^{pair}. The resulting potential curves for the states $6p\ ^2\Sigma_{1/2}$, $6p\ ^2\Pi_{1/2}$, and $6p\ ^2\Pi_{3/2}$ are shown in Fig. 1 as red lines. The energy of the ground state $6s\ ^2\Sigma_{1/2}$ is plotted as a blue curve.

B. Atomic bubble model

The atomic bubble model was introduced for the first time by Hickman *et al.*[30] in their study of excited He atoms in liquid helium. The theory was then extended for alkaline-earth atoms and ions by Bauer *et al.*[5] It was also successfully applied to many other neutral dopants such as reviewed in Ref. 8. Here we develop the atomic bubble model for Ba^+ in liquid He, using *ab initio* Ba^+-He pair potentials[7,23,26] that are expected to be more accurate than those used by the authors of earlier calculations.[5]

$$E_{tot} = E_{Ba^+}^{\text{free}} + \int \rho(\mathbf{R}) \Delta V^{pair} d^3\mathbf{R} + E_{liq} \quad (2)$$

The total energy of the ion in liquid helium can be written as a sum of pair-interactions weighted by the liquid helium density plus the energy that is needed to form a bubble in the liquid, E_{liq}. We denote $\Delta V^{pair} = V^{pair}(R) - V^{pair}(+\infty)$. For nonspherical bubble geometries the hamiltonian is

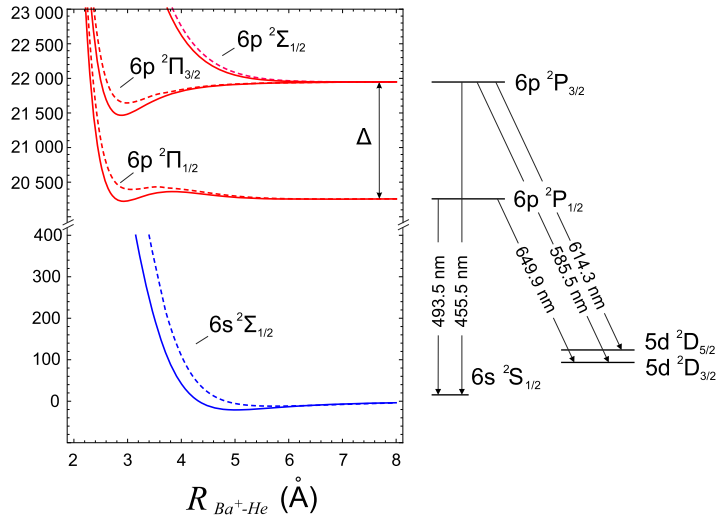

FIG. 1. Left side: Adiabatic Ba^+-He pair-potentials with the spin-orbit interaction included. Dashed curves - pair potentials taken from Ref. 23, solid curves - pair potentials taken from Refs. 7 and 26. Right side: Energy levels and electronic transitions of a free Ba^+ ion.

constructed by integration over the pairs with the appropriate rotation matrices applied.[8] The liquid helium is treated as a continuous medium even at a nanometer scale. We assume that the energy of the liquid, E_{liq}, consists of three terms: a pressure-volume work E_{PV}, an energy due to the surface tension E_S, and a volume-kinetic energy E_{Vk}.[31] E_{liq} can be written as:

$$E_{liq} = E_{PV} + E_S + E_{Vk} = pV_{bubble} + \sigma S_{bubble} + \frac{\hbar^2}{8M_{He}} \int \frac{(\nabla\rho(\mathbf{R}))^2}{\rho(\mathbf{R})} d^3\mathbf{R}, \tag{3}$$

where M_{He} is a mass of a He atom.

Density distribution of He atoms $\rho(\mathbf{R})$ around the ion is modeled by a trial function. We assume that Ba^+ forms a bubble and use the same trial function $\rho(\mathbf{R})$ as was used in Ref. 5 and other works on atomic bubbles (see Ref. 8).

$$\rho(R, R_0, \alpha) = \begin{cases} 0, & R \le R_0 \\ \rho_0[1 - \{1 + \alpha(R - R_0)\}e^{-\alpha(R-R_0)}], & R \ge R_0, \end{cases} \tag{4}$$

here, ρ_0 is a liquid helium number density at a given temperature and saturated vapor pressure, $1/\alpha$ and R_0 correspond to the bubble interface thickness and the bubble radius, respectively.

Pressure-volume work and the energy due to the surface tension depend on the characteristic radius R_b of the bubble. The interface of the bubble is not sharp and the effective bubble radius R_b, is obtained from the equation of center of gravity of the bubble interface profile:

$$\int_0^{R_b} \rho(R) \cdot 4\pi R^2 dR = \int_{R_b}^{+\infty} [\rho_0 - \rho(R)] \cdot 4\pi R^2 dR. \tag{5}$$

Then the energy of liquid helium can be rewritten as

$$E_{liq} = \frac{4}{3}\pi p R_b^3 + 4\pi\sigma R_b^2 + \frac{\pi\hbar^2}{2M_{He}} \int_0^{+\infty} \frac{(\nabla\rho(R))^2}{\rho(R)} R^2 dR. \tag{6}$$

Finally, the total energy of Ba^+ ion in liquid helium can be written:

$$E_{tot} = E_{liq} + E_{Ba^+}^{\text{free}} + 4\pi \int_0^{+\infty} \rho(R)\Delta V^{pair} R^2 dR. \tag{7}$$

Surface tension σ, saturated vapour pressure p, and the corresponding density of liquid helium ρ_0, at T = 1.6 K were taken from literature.[32–34]

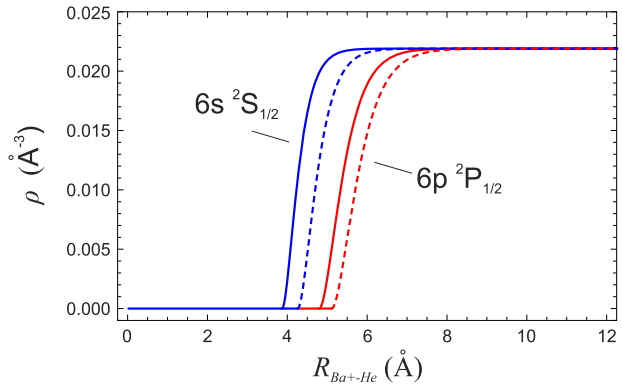

FIG. 2. Radial distributions of liquid He density around the Ba^+ ion for Ba^+ $6s\ ^2S_{1/2}$ and $6p\ ^2P_{1/2}$ states. Trial density distribution function, Eq. (4). Solid curves are for the pair-potentials from Refs. 20 and 23, dashed curves are for the pair-potentials from Refs. 7 and 26.

The minima of the total energies, E_{tot}, for the ground $6s\ ^2S_{1/2}$ and excited $6p\ ^2P_{1/2}$ states of Ba^+ in liquid helium are found by numerical method using *Mathematica 9* software package. In this way we obtain the parameters R_0 and α corresponding to the equilibrium configuration of the bubble. Resulting radial distributions of liquid helium density are shown in Fig. 2.

C. A model of oscillating bubble

In order to calculate spectral linewidth, we use the model of oscillating bubble. Motion of He atoms surrounding Ba^+ ion perturbs the bubble interface and thus the total energy is changed which leads to the broadening of the spectral line. The complex motion of the bubble interface can be treated as a sum of vibration modes: radial shrinking and expansion of the bubble (breathing mode), relative motion of the bubble center and the ion (dipole mode), and higher order modes (quadrupolar and etc.).

In this section we calculate the effect of the breathing mode. The deformed bubble model is introduced in the following section.

The change of the bubble size and corresponding perturbation of the total bubble energy is found in the same way as described in Ref. 8 and 35. The probability to find a bubble with a radius R is given by a wavefunction $\Psi^B(\mathbf{R})$. It is found as the solution of the one-dimensional Schrödinger equation for the bubble with an effective mass $M^B_{\mathbf{eff}} = 4\pi R_b^3 \rho_0$.

$$[-\frac{\hbar^2}{2M_{\mathbf{eff}}}\ \nabla^2 + E_{tot}(\mathbf{R})]\Psi^B(\mathbf{R}) = E_{vib}\Psi^B(\mathbf{R}) \tag{8}$$

The calculations have shown that the splitting between the ground vibrational state and the first excited state is approximately 12 K for Ba^+ $6s\ ^2S_{1/2}$ and 8 K for $6p\ ^2P_{1/2}$ states. Therefore, in the temperature range of T = 1.6–2.1 K around which our experiments are performed, we can take into account only the lowest level.

In Fig. 3 the excitation-emission cycle is shown. According to the Franck-Condon principle, during the electronic transition the bubble shape and radius do not change. Then the bubble relaxes to a new equilibrium state that is characterized by different values of parameters α and R_0. The lifetime of the $6p\ ^2P_{1/2}$ state for the free Ba^+ ion is 7.9 ns.[36] Typically, the lifetimes of electronically excited states of an atom embedded in liquid helium are shorter than in a free atom by a few percent.[8,37] The bubble thus has sufficient time to adopt its shape and size to the new electronic state. The fluorescence occurs in the larger bubble and brings the system from the excited state to the ground state. After that, the bubble relaxes to the initial configuration.

The absorption lineshape, $P^B(E)$, is given by a projection of the probability distribution $|\Psi^B(\mathbf{R})|^2$ onto the potential curve of the excited state. A similar procedure is applied to calculate the emission spectrum for the transition from the excited $^2P_{1/2}$ state to the ground state. As discussed in Ref. 38, the discrete structure of the vibronic states can not be seen in the spectra due to the fact that the bubble

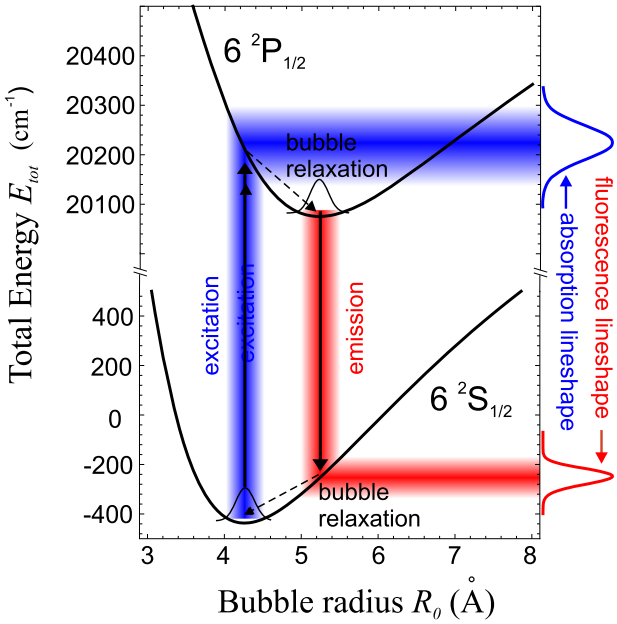

FIG. 3. Energy diagram and excitation-emission cycle of Ba^+ D_1 transition ($6s\ ^2S_{1/2}$ - $6p\ ^2P_{1/2}$). Potential energy curves are drawn for the fixed parameter $\alpha = 3.5$ Å^{-1}. Black up and down arrows indicate electronic transitions for the D_1 excitation and emission of Ba^+, respectively. The shaded bands visualize the delocalization of the bubble interface and the corresponding line broadening. The energy diagram is obtained using the pair-potentials from Ref. 23.

relaxation (expansion or shrinking) following the electronic transition proceeds on the picosecond time scale, comparable to the period of the bubble vibrations. A strong coupling between bubble vibrations and phonons lead to overlapping of the neighboring quantum states and to the continuous excitation/emission spectrum.

D. Deformed bubble model

Quadrupolar modes lead to a deformation of the bubble surface and to the additional line broadening. In this subsection we extend the SBM to the deformed bubble model (DBM) following the approach developed in the paper.[35] The radius of the bubble, R_S, depends on the polar angles Θ and Φ and is expanded in terms of spherical harmonics.

$$R_S(R_0, \Theta, \Phi) = R_0 + \sum_{i=1}^{\infty} \sum_{j=-i}^{i} R_{ij} Y_i^j(\Theta, \Phi), \tag{9}$$

where index i runs from 1 to ∞ and j from -i to i.

In Eq. 9, the first term, R_0, is the radius of a spherical bubble and the other terms represent deformation of this sphere. For example, terms with i=1 correspond to dipole modes (translation of a bubble) and terms with i=2 to quadrupolar modes. For the quadrupolar modes there are six independent parameters R_0 and R_{2j} (j = -2, ...,2). We transfer the coordinate system to the system where the axes match the principal axes of the deformed bubble.[35] In this coordinate system, the deformation of the bubble shape can be written as:

$$R'_S(R_0, \Theta', \Phi') = R_0 + R'_{20} Y_2^0(\Theta') + R'_{22}[Y_2^2(\Theta', \Phi') + Y_2^{-2}(\Theta', \Phi')]/\sqrt{2} \tag{10}$$

Under this transformation, the origin of the system and R_0 remain unchanged but the bubble is rotated. It has been shown that the energy of the bubble rotation can be neglected during a period of the surface oscillations.[35] The density distribution around the ion can be written as described in Sec. II replacing R_0 by R_S in Eq. 4:

$$\rho(R, \Theta, \Phi) = \begin{cases} 0, & R \le R_0 \\ \rho_0[1 - \{1 + \alpha(R - R_S)\}e^{-\alpha(R-R_S)}], & R \ge R_S, \end{cases} \tag{11}$$

TABLE I. Equillibrium parameters of the atomic bubble obtained from ABM for the different Ba^+-He pair-potentials. R_{0eq} - radius of the bubble, α_{eq} - inverse bubble interface thickness, R_b - characteristic radius of the bubble.

$6s\ ^2S_{1/2}$			$6p\ ^2P_{1/2}$			
R_{0eq}, Å	α_{eq}, $Å^{-1}$	R_b, Å	R_{0eq}, Å	α_{eq}, $Å^{-1}$	R_b, Å	Pair-potentials
4.3	3.5	4.8	5.1	2.6	5.9	[23]
3.9	4.3	4.3	4.8	2.9	5.5	[7,26]

We assume that both breathing and quadrupolar oscillations are induced independently at the same time. The bubble shape is determined by the amplitudes R_{20}, R_{22} and parameters R_0, α. Since we consider only small quadrupolar oscillations, equilibrium parameters R_0 and α obtained from SBM are also used in DBM. Their values are listed in Table I.

Surface energy and the pressure-volume work can be written as follows[30,39]

$$E_S = [4\pi R_b^2 + 4R_b^2(R_{20}^2 + R_{22}^2)/R_0^2]\sigma, \tag{12}$$

$$E_{PV} = [\frac{4}{3}\pi R_b^3 + 4R_b^3(R_{20}^2 + R_{22}^2)/R_0^2]P, \tag{13}$$

where R_b is the effective bubble radius obtained by SBM calculations.

The energy surfaces of the ground $^2S_{1/2}$ and excited $^2P_{1/2}$ states are obtained as a sum of the interaction and bubble energies, similar to Eq. 2. For a relevant range of the amplitudes R_{20}, R_{22}, they are shown in Fig. 4.

The energy surfaces $E_{tot}(R_{20}, R_{22})$ plotted in Fig. 4 were fitted by two-dimensional harmonic potentials. The effective mass for quadrupolar oscillation modes is given by $M_{eff}^Q = R_b^3\rho_0 M_{He}/3$. Then the wave functions $\Psi^Q(\boldsymbol{R})$, are obtained by solving two-dimensional Schrödinger equation. For the quadrupolar modes, the energy intervals between the two lowest vibronic states are 24 K for the ground state and 14 K for the excited state. These energies are much larger than the thermal energy in the experiment (T = 1.6–2.1 K). We therefore assume that the optical transition occurs only from the ground quadrupolar state.

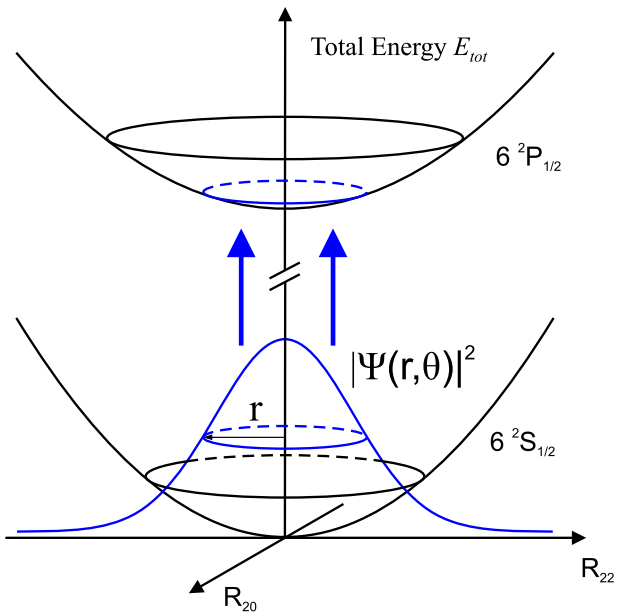

FIG. 4. Energy diagram for the Ba^+ D_1 transition (excitation) perturbed by quadrupolar bubble oscillations. Potential energy surfaces are plotted for the fixed parameters α and R_0 obtained from ABM and corresponding to $6s\ ^2S_{1/2}$ state. For clarity, calculated potential energy surfaces for the D_1 emission are not drawn.

TABLE II. Spectral lineshifts and linewidths of Ba^+ in liquid ^4He. δ^{exp}, γ^{exp} - experimental[2] line shift and width, δ^{exp}, γ^{th} - calculated line shift and width obtained using different sets of *ab initio* pair potentials.

		Ba^+ in LHe, bubble model (BM)					
		Ba^+ in LHe, experiment[2]		MRCI, Ref. 23		CCSD(T), Refs. 7, 26	
D_1 Transition	Free Ba^+ (cm^{-1})	δ^{exp} (cm^{-1})	γ^{exp} (cm^{-1})	δ^{th} (cm^{-1})	γ^{th} (cm^{-1})	δ^{th^*} (cm^{-1})	γ^{th} (cm^{-1})
Fluorescence	20 262	+105	83	+141	38	+108	51
Absorption	20 262	+485	194	+373	91	+421	93

The line profile for the quadrupolar modes is obtained by projection of the probability distribution of the initial state to the potential surface of the final state assuming that the bubble configuration doesn't change during the optical transition. For the fixed transition energy, E, various deformed bubble configurations are possible. In general case the amplitudes R_{20} and R_{22} corresponding to these deformations are distributed in an ellipse. Then, in order to obtain the line profile $P^Q(E)$, we express polar radius r as a function of E and Θ and integrate over the polar angle weighted by the probability distribution:

$$P^Q(E) = \int_0^{2\pi} |\Psi^Q[r(E,\theta)]|^2 r(E,\theta) d\theta. \tag{14}$$

The total line profile of the transition is calculated as a convolution of normalized breathing and quadrupolar line profiles:

$$P(E) = \int_{-\infty}^{+\infty} P^Q(E - E') P^B(E') dE', \tag{15}$$

where $P^B(E')$ - line profile obtained using atomic bubble model when only the breathing mode is taken into account.

The wavenumber for the free Ba^+ D_1 transition, lineshifts, δ^{th} and FWHM linewidths, γ^{th}, of the excitation and emission spectra of the optical transition in bulk liquid helium are listed in Table II.

III. EXPERIMENT

A. Ion production

In order to immerse impurity ions in liquid helium different techniques were developed in the past.[3,24,40–42] It is possible to create the ions by means of laser ablation. When the ablation target is immersed in liquid helium, a small vapor bubble is formed around the ablation spot. The ablation products are confined in this bubble, that leads to a strong ion-electron recombination.[17] Another process reducing the number density of injected ions is the clusterization of ions and neutral atoms and the formation of charged clusters and nanoparticles. In a series of preliminary experiments we have applied a second pulsed laser for the dissociation of the clusters[43,44] and for the ionization. However, this did not improve the ion yield.

Although one may use large static electric field of order of several kV/cm to extract the ions from plasma bubble into liquid helium,[24,42] this method is inefficient to immerse charged dopants. Thus it is mostly used to immerse neutrals.[8] On the other hand, laser ablation in the gas phase above the liquid He surface has successfully demonstrated that the ions can be injected inside liquid helium.[13,31] In this case, the ion yield may be further increased by ionization of neutral Ba atoms by electric discharge in the gas above the liquid surface.[40,41] The latter method is applied in the present experiment.

The top view of the experimental set-up is shown in Fig. 5(a). A cylindrical copper cell with glued four sapphire windows is installed in the sample chamber of a commercial optical cryostat. The sample chamber is filled with liquid ^4He and is cooled down to T=1.6-2.1 K by pumping on the liquid He surface. The vertical cut through the cell is shown in Fig. 5(b). A helical radio frequency (r.f.) resonator and a He transfer line are mounted at the top cap of the cell. The second harmonic of a pulsed Nd:YAG laser is introduced through the one of the side windows and is focused on the Ba target with a f=10 cm lens. The laser parameters are λ = 532 nm, repetition rate 1-10 Hz, pulse

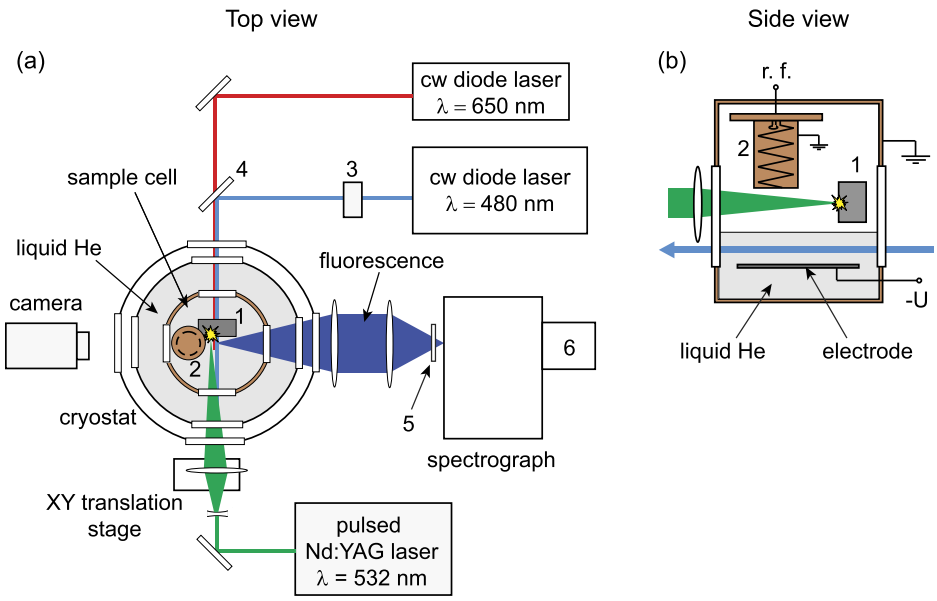

FIG. 5. Experimental setup: a) top view of the cryostat and optical setup, b) vertical cut through the cell. 1 - ablation target, 2 - helical r.f. resonator, 3 - AOM, 4 - dichroic mirror, 5 - interference filter suppressing scattered laser light, 6 - CCD camera.

energy 1-25 mJ, and pulse width 5 ns. The cell walls, the target, and the walls of the helical resonator are grounded. Ba atoms and Ba^+ ions are produced by laser ablation of Ba metal in He gas above the liquid surface. A radio frequency discharge is used to ionize the neutral Ba atoms created by the laser ablation and therefore to increase the ion number density in the gas. The discharge is produced inside the helical resonator that has an open lower end and is driven at it's self-resonant frequency of 430 MHz. The r.f. power is square-wave modulated at a repetition rate of f_{dis} that is varied in a range from 0.5 Hz to 2 kHz, with a duty cycle of 0.01 - 0.5. The output power of the r.f. amplifier could be varied in the range of 0-190 W, although it is difficult to ascertain the power that was actually dissipated by the plasma. The parameters of the discharge were adjusted to find a compromise between the heating inside the cell and the Ba^+ ion yield.

The efficiency of the Ba^+ production was monitored by recording the spectra of light emitted by the discharge and measuring the relative intensities of spectral lines belonging to He atoms, Ba atoms, and Ba^+ ions. Typical spectra of the plasma emission are plotted in Fig. 6. With the ablation laser shooting at a repetition rate of several Hz, certain steady-state number density of Ba atoms inside the helical resonator was established. Under those conditions, the synchronization between the ablation and r.f. pulses become unimportant and we could adjust the ablation rate and the r.f. pulse rate independently.

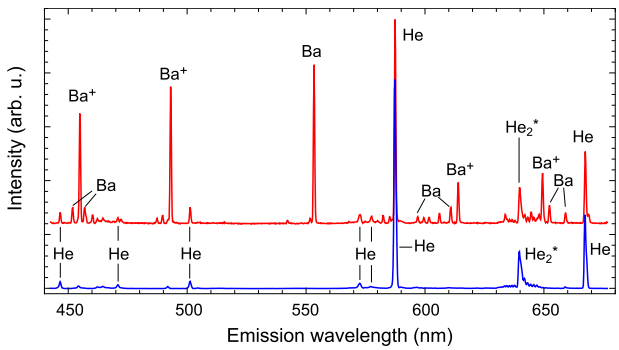

FIG. 6. Typical emission spectra of He-Ba r.f. plasma above a free surface of superfluid He. T = 1.65 K, f_{dis}=5 Hz, τ_{dis}=50 μs, r.f. power 190 W. Upper (red) curve - ablation laser on, lower (blue) curve - ablation laser off.

This method has produced a large amount of Ba^+ ions which diffuse out of the r.f. resonator and can be excited by a cw laser radiation.[22] By measuring the absorption of the laser light resonant with the $6^2S_{1/2} - 6^2P_{3/2}$ transition of Ba^+ ($\lambda = 455.4$ nm) in the He gas below the resonator, we have obtained the ion number density of $\approx 10^{10}$ cm^{-3}.

A horizontal disc electrode (Fig. 5(b)) is placed in liquid He at a 10 mm distance below the target in order to create a vertical electric field and induce the drift of the ions towards the surface of liquid helium. The ions move towards the electrode in a static electric field, typically, $E_\perp = 1.0$ - 3.5 kV/cm, applied between the electrode and the target.

Oxidation of the target surface is a common problem in laser ablation experiments. Although appropriate precautions are taken before and after mounting the ablation target in the sample cell, an oxide layer appears at the surface of metallic barium. Before cooling the cryostat, the sample cell is filled with He gas and the target surface is cleaned by pulsed Nd:YAG laser operated at a 10 Hz repetition rate, and with pulse energy of 20 mJ. Two motorized translational stages are used to move the lens (Fig. 5(b)) in the plane orthogonal to the laser beam. The beam is focused some millimeters behind the target surface in order to have not too small spot size. The ablation spot moves along the barium surface following the programmed movements of the translation stages. The process is monitored by a video camera protected from the intense scattered laser light by an interference filter. After the removal of the oxide layer, we can operate the laser at a much lower power during the low temperature experiment and prevent overheating of the sample cell. Typically, in the course of the experiment at low temperature the ablation laser pulse has the energy of 0.4 - 1.5 mJ. The laser beam is tightly focused on the target surface and the ablation spot is moved along the cleaned part of the surface by the same opto-mechanical system. The size of the ablation spot was ≥ 4 μm in diameter (calculated for the Gaussian beam). Every ablation pulse thus hits a fresh spot on the surface. This prevents the hole-drilling effect and greatly improves the stability of the ion yield.

B. Spectroscopy

A cw frequency-doubled diode laser is used to excite the Ba^+ ions in liquid helium several millimeters below the liquid helium surface. It is tuned to 482 nm, to match the wavelength of the $6^2S_{1/2}$-$6^2P_{1/2}$ (D_1) absorption line of Ba^+ in liquid He ($\lambda = 493.5$ nm in a free ion). The power of the laser, typically, was set to 20-200 mW. At high power, this laser induces a noticeable heating of the sample cell by some 10–20 mK. In order to reduce the heating effect, in some experimental runs the laser beam was modulated on-off by an acousto-optical modulator (AOM) with a repetition rate of 1 Hz and a duty-cycle of 0.1 - 0.01 %.

The fluorescence light is collected from the side window of the cryostat and focused on the entrance slit of a grating spectrograph Acton SP2300 (grating 1200 g/mm blazed at 500 nm, 0.14 nm resolution) equipped with a CCD camera PIXIS 100BR (matrix size 1340×100 pixels) made by Princeton Instruments.

A significant proportion of the ions excited to either of the two $6^2P_{1/2,\,3/2}$ states decays towards the metastable $5^2D_{3/2,\,5/2}$ states (see Fig. 1). In order to repump these ions back into the $6^2P_{1/2}$ state, we introduce a second cw laser beam resonant with the $5^2D_{3/2} - 6^2P_{1/2}$ transition at $\lambda = 649.7$ nm. It is produced by a cw diode laser with the maximum output power of 30 mW. The beam is superimposed with the primary excitation beam by using a dichroic mirror, as shown in Fig. 5(a). When applied to Ba^+ ions in the He gas below the r.f. resonator, the repumping significantly increases the yield of the laser-induced fluorescence at the $6^2S_{1/2} - 6^2P_{1/2}$ transition. However, no significant increase of the fluorescence yield was observed in the liquid He. Since the exact wavelength of the $5^2D_{3/2} - 6^2P_{1/2}$ (repumping) transition of Ba^+ in liquid He is not known, it is possible that the repumping was inefficient due to the wavelength mismatch.

Typical spectrum of the laser-induced fluorescence generated in liquid He several mm below the free surface is shown in Fig. 7. The D_1 emission line is blueshifted by 2.4 nm (105 cm^{-1}) with respect to the transition in a free ion. The full width at half-maximum (FWHM) linewidth is 2.0 nm (83 cm^{-1}). The center wavelength of the observed emission line agrees with $\lambda = 491$ nm reported in Ref. 2. In that experiment, the resolution of a monochromator was equal to 6.6 nm and a deconvolution technique was applied in order to obtain $\Delta\lambda$ from the measured data. The resulting FWHM linewidth is also in agreement with our results.

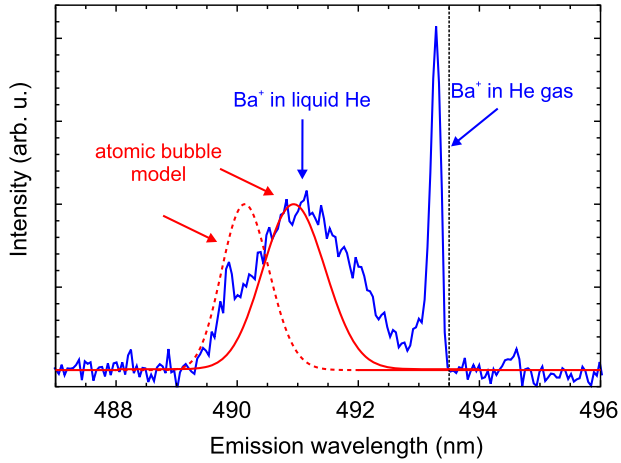

FIG. 7. Observed emission spectrum of Ba^+ ions in superfluid He. D_1 ($6p\ ^2P_{1/2}$ - $6s\ ^2S_{1/2}$) transition, T = 2.13 K, ablation at 10 Hz, f_{dis} = 3.3 kHz, τ_{dis} = 10 μs, $E_\perp$ = 3200 V/cm. Red curve is a calculated spectrum of Ba^+ in liquid He according to the atomic bubble model (solid curve for pair potentials,[7,26] dashed curve for pair potentials[23]). Vertical dashed line indicates the wavelength of the D_1 transition in a free ion.

In Fig. 7 one can also see the fluorescence of Ba^+ from the gas phase which appears as a sharp line at λ=493.4 nm. The wavelength within resolution matches the transition of the free Ba^+ ion. This emission most likely comes from the r.f. plasma at the open end of the helical resonator. We thus can unambiguously distinguish the emission of the solvated ions from that of the ions in the gas phase.

C. Electric breakdown in superfluid He

The spectroscopic measurements were carried out in the temperature range of T = 1.6–2.2 K. The strongest fluorescence signal from solvated ions is observed slightly below the λ-point at 2.17 K. Its intensity strongly decreased above 2.17 K, most likely because of boiling of liquid He in the cell and in the bath and strong scattering of the laser light. Below 2.17 K, the fluorescence was observed down to T = 2.0 K. The decrease of the injection efficiency at lower temperature is surprising since the saturated vapor density is decreasing with temperature and therefore the ions produced in the gas phase should experience smaller number of collisions with gas atoms on their way to the liquid surface. The observed effect therefore should be related to the temperature and pressure dependence of the ion yield in the r.f. gas discharge.

As the temperature is lowered further, down to T = 1.6–1.7 K, the fluorescence signal from the solvated Ba^+ ions is recovered. At this temperature, the applied static electric field in excess of 1.5 kV/cm in the presence of Ba-He r.f. plasma induces a breakdown in superfluid He. The breakdown occurs only when both the ablation laser and the r.f. discharge are switched on. We observe a pulse of electric current registered by the high voltage power supply, accompanied by a bright flash of the discharge and a sudden large splash or a fountain of liquid helium in the cell. Ejected liquid He rises above the cell windows and reaches the ablation target, the helical r.f. resonator, and even the ceiling of the cell. The discharge is self-terminated within some 100 ms, probably because of liquid He disrupting the conducting gas (plasma) channel between the grounded parts of the setup and the high-voltage electrode. With all conditions fixed, we observe these breakdown/splash events occurring at irregular intervals of 50–200 s.

The spectrum of the emitted light flash contains all the same spectral lines of He and Ba atoms, He_2^* excimer, and Ba^+ ion, as observed in the spectrum of the r.f. discharge in the gas phase (see Fig. 6). The effect is illustrated in Fig. 8, where we plot the time-dependent intensities of the two lines at 493.4 nm and 491 nm, corresponding to the gas-phase and solvated Ba^+ ions, respectively. The intensities of ablation and excitation lasers, as well as the applied high voltage and the parameters of the r.f. discharge were kept constant during the recording. Each point represents a 2 s exposure time. One can see 6 breakdown events that have occurred within 300 s. The intensity of the gas-phase signal is strongly enhanced within 10 s time intervals following each event. This emission could

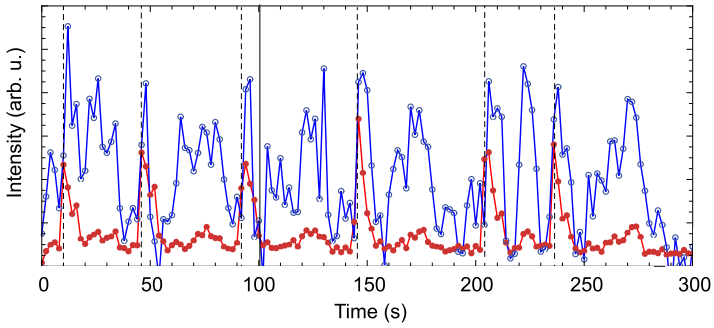

FIG. 8. Observed time-dependent intensity of Ba^+ D_1 fluorescence. Open circles (blue) - signal from solvated ions in superfluid He at λ = 491 nm; filled circles (red) - signal from gas bubbles or from He gas above the liquid at λ = 493.4 nm. T = 1.7 K. Vertical dashed lines indicate breakdown events.

originate from Ba^+ ions trapped in gas bubbles created by the splash in liquid He. The intensity of the emission from solvated Ba^+ ions strongly fluctuates between the events. However, it decreases to zero just before every splash and quickly rises within 1 s after it.

No fluorescence from solvated ions could be observed at T = 1.6–1.7 K in the absence of these breakdowns/splashing, *i.e.* with the static electric field below the breakdown threshold, without r.f. discharge, or with insufficient r.f. power. We therefore conclude that the ions become injected into superfluid He as a result of these splashes and/or large electric current flowing to the collector.

No significant heating of the sample cell or increase of the He pressure was observed as a result of the breakdown. However, the local conditions in the He-Ba plasma may not be represented by the readings of the temperature sensor in the He bath and the pressure gauge at the warm part of the He filling line. We also note that the breakdown threshold decreases significantly with time during the operation of the plasma and ion source, probably due to the accumulation of charges in the cell. This makes the systematic study of the breakdown much more complicated and the quantitative data much less reliable.

IV. DISCUSSION

A. Line shift and broadening

In Fig. 7 the calculated D_1 emission spectra of Ba^+ are compared with the experimental data obtained at T = 1.6 K. Two calculated lineshapes correspond to the different sets of ab initio Ba^+-He pair potentials,[7,23,26] as discussed in Sec. II. Transition lineshifts δ and FWHM linewidths γ of the calculated and measured spectra are listed in the first line of Table II. The line shift with respect to the free ion δ^{th} is equal to +141 and +108 cm^{-1} for the calculated spectra and δ^{exp} = +105 cm^{-1} for the experimental data. The calculated linewidth γ^{th} is equal to 38 and 51 cm^{-1}, respectively, whereas the experimental value is γ^{exp} = 83 cm^{-1}. The agreement is significantly better for the CCSD pair potentials.[7,26] The atomic bubble model thus overestimates the shift of the emission line only by 3% and underestimates the broadening by a factor of 1.6.

In our experiment, the absorption spectrum was not investigated. In Fig. 9 the calculated excitation spectra are compared with the experimental data of Refs. 2 and 15. The corresponding lineshifts and FWHM linewidths are listed in the second line of Table II. The agreement is better for the CCSD pair potentials,[7,26] especially in the line shift. As discussed in Sec. II, both the line shift and the line broadening are more pronounced in the excitation spectra than in the fluorescence. The calculation again strongly underestimates the line broadening: γ^{th} = 93 cm^{-1} vs. γ^{exp} = 194 cm^{-1}. The shift is underestimated by 15%: δ^{th} = +421 cm^{-1} vs. δ^{exp} = +485 cm^{-1}.

The main contribution to the calculated spectral widths and shifts comes, as expected, from the breathing vibrations (fluctuations) of the bubble. The quadrupolar vibration modes lead to additional minor line broadening of 5.5 cm^{-1} in absorption and 0.5 cm^{-1} in emission for the pair potentials[23] and of 2.6 cm^{-1} in absorption and 0.3 cm^{-1} in emission for the pair potentials.[7,26] The spectral line shapes due to the quadrupolar modes are strongly asymmetric. They therefore induce a noticeable

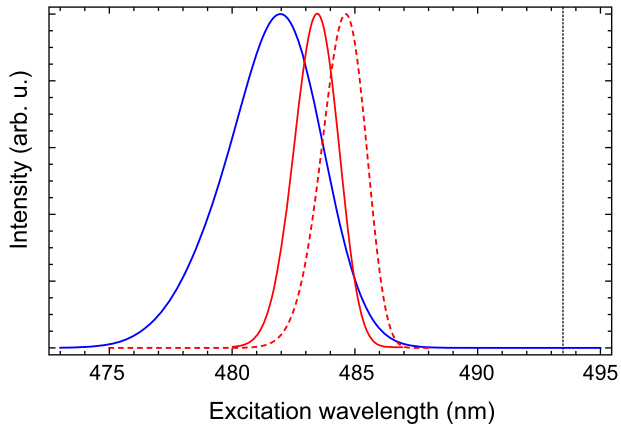

FIG. 9. Absorption spectrum of Ba^+ D_1 transition in liquid He. Red line - present ABM calculations (solid curve for pair potentials,[7,26] dashed curve for pair potentials[23]), blue line - experimental data from Ref. 2. Vertical dashed line indicates the wavelength of the D_1 transition in a free ion.

shift of the resulting lineshapes by +14.0 cm^{-1} in absorption and by +1.5 cm^{-1} in emission for the potentials[23] and by +7.7 cm^{-1} in absorption and by +1.7 cm^{-1} in emission for the potentials.[7,26] We do not take into account the dipolar vibration modes, *i.e.* the oscillations of the ion with respect to the center of the bubble, since their contribution is expected to be even smaller.[24]

We can compare our results to other existing atomic bubble calculations[5,24] for ionic species. In the earlier work[5] on Ba^+ in liquid He, only the absorption spectrum of the D_1 transition was calculated. That calculation underestimated the line shift by 40%, whereas the line broadening was in a good agreement with the experiment, underestimated by only 10%. The other impurity ion, for which the spectroscopic data is available is Yb^+. Both, the excitation and emission spectra of the $4f^{14}6s\ ^2S_{1/2}$ - $4f^{14}6p\ ^2P_{1/2}$ transition have been reported.[24] This transition is analogous to the D_1 line of Ba^+, although Yb^+ possesses also a $4f$ inner electronic shell. The calculations[24] strongly overestimated the line shift both in absorption (by 85%) and in emission (by 133%). The line broadening is underestimated by 10% in absorption and by 62% in emission, respectively. The data are not sufficient for inferring any definite trend. It is not clear, to what extent these discrepancies can be attributed to the inaccuracy of the interatomic pair potentials and to the shortcomings of the bubble model.

B. Trapping site structure

We have carried out our atomic bubble calculations in order to answer the old question:[4,5] how well the atomic bubble model represents the structure and the energetics of the trapping site of the ion. The merits of this model are it's simplicity and a straightforward physical interpretation of the observed effects. However, the bubble model was developed for impurities with purely repulsive impurity-helium interaction, such as neutral alkali-metal atoms. It therefore does not allow for the shell-structure formation that is typical for the ions because of the attractive polarization interaction. Our results show that for Ba^+ the atomic bubble model is in a qualitative agreement with the experimental spectroscopic observations. As expected, the agreement is not as good as in the case of neutral alkali-metal atoms Cs and Rb.[8,35,45] In the future, it will be interesting to investigate the dependencies of the ionic spectra on the helium pressure and temperature and to check whether they agree with the predictions of the bubble model, as it was demonstrated for the alkalis.[8,45]

The DFT calculations[6,7] demonstrate that the more realistic He density profile around the Ba^+ ion has a pronounced maximum, corresponding to a high-density solid-like shell surrounding the bubble. The "snowball" structure is formed due to the combination of the attractive force acting on He atoms due to the ion-dipole interaction and the repulsive force due to the exchange interaction with the remaining valence electron of a singly-ionized Ba. The absorption spectrum of the D_1 transition calculated by DFT methods in Ref. 7 overestimates the broadening and slightly underestimates the lineshift measured in Ref. 2. Our atomic bubble calculations underestimate both, the linewidth and

lineshift for the absorption spectrum. The emission spectrum of the same transition calculated by DFT methods in Ref. 16 underestimates both, the broadening and the lineshift observed by us and earlier by Reyher *et al.*[2] Our atomic bubble calculations give a better result for the lineshift, but underestimate the linewidth for the emission spectrum. In our experiments we don't see the emission at the wavelength λ=523 nm^2 and attributed to barium exciplex formation.[16]

The valence electron of a single-charged Ba^+ ion occupies a rather large volume. The repulsive interaction between this electron and the electronic shells of He atoms dominates at the distances of up to 5 Å. The potential curves of Fig. 1 are therefore quite similar to those of neutral metal atoms. The potential well due to the attractive polarization interaction is very shallow and does not significantly affect Ba^+-He interaction. It is therefore not surprising that the bubble model successfully captures the main properties of the trapping site and the resulting spectra. The high-density He shell is located rather far from the ion and it's effect on the energetics of the electronic transition is rather small. Both, DFT and the bubble model predict a much tighter trapping site for the electronic ground state of the ion than for the excited state. This leads to a much more pronounced energetic shift of the absorption spectrum as compared to the emission spectrum. The magnitude of the shift is calculated with a satisfactory accuracy by both models. The remaining discrepancy can be attributed to the imprecision of the used pair potentials.

The broadening of the transition and the shape of the spectrum are determined by the quantum fluctuations of He atoms surrounding the ion. The bubble model represents them as a superposition of the bubble vibration modes, calculated accordingly to classical hydrodynamics. One could imagine that the presence of a solid shell around the bubble should reduce the magnitude of it's vibrations and thus make the linewidth smaller. In fact, the opposite happens. Our results show that the bubble model underestimates the broadening by a factor of 2, although the shape of the spectrum is quite close to that observed experimentally. We therefore conclude that the high-density shell surrounding the bubble significantly affects its fluctuations in a counterintuitive manner. A question remains, whether these fluctuations can be described in terms of some collective modes characteristic for a hollow spherical shell submerged in a liquid.

C. Injection of Ba^+ into superfluid He

At the moment, we do not have a clear interpretation of the electric breakdown phenomena described in Sec. III. The fact that no solvated ions could be observed at the electric field strength lower than ≈ 1.5 kV/cm seems to indicate that there exists an energetic barrier for the ion penetration into the liquid. This conclusion is supported by the observation of a quasiperiodic explosion-like electric breakdown at $T \leq 1.7$ K. The charges seem to accumulate above the free surface of the liquid until their surface density exceeds certain threshold. A surface instability then develops leading to a local depression of the liquid, formation of a bubble or a gas channel reaching the surface of the negatively charged electrode and finally a breakdown. Similar instability and formation of charged bubbles was investigated both theoretically and experimentally in connection with free electrons trapped above the free surface of superfluid He,[46–49] although no explosion-like breakdown was reported.

On the other hand, the injection of Ba^+ into superfluid He under the experimental conditions that are very close to those of the present work was successfully demonstrated in Ref. 2 at a much smaller electric field strength. The DFT calculations of Ref. 7 reveal no barrier for the solvation of Ba^+ in liquid He and the experimental observations of Ref. 15 indicate that the ion sinks into a superfluid He nanodroplet without any external electric field.

Our own study[50] has demonstrated that under the conditions of the present experiment a space charge-limited electric current is flowing in liquid He and across the liquid-gas interface. Under the strong vertical static electric field applied in the present experiment, this current reaches 2–5 μA, which corresponds to the ion number density of order of 10^9 cm^{-3}. This is a large density that is comparable to the typical densities of neutral impurity atoms that could be injected into liquid or solid He and is also comparable with the number density of Ba^+ ions that we have detected in the He gas just below the open end of the r.f. resonator. The electric current measurements can not discriminate between Ba^+ and He^+ ions. However, the current observed in the absence of Ba, with the ablation laser switched off is significantly lower than that in the presence of Ba, under otherwise identical

conditions. We therefore expect that a large amount of Ba^+ is injected into superfuid He in the present experiment.

The poor yield of the laser-induced fluorescence from Ba^+ and its total absence under the electric field strength below 1.5 kV/cm is still surprising. Similar situation was encountered in ref. 51, where it was believed that a large quantity of Ba^+ ions was injected in liquid and solid He, but no laser-induced fluorescence of Ba^+ could be detected at all. One possible explanation is that the ions entering the liquid He in the present experiment are efficiently captured by Ba metal filaments and nanonetworks attached to the bottom electrode and having the same (negative) electric potential. The presence of such filaments, networks, and tree-like structures in our sample cell has been established by visual observations and by a microscopy study.[50,52] They appear as a result of the coalescence of the ablation products (neutral or charged) in superfluid He and at the liquid-gas interface. Another possibility is that the dominant charged species are not single Ba^+ ions, but some molecular or cluster-ions Ba_n^+, or Ba^+ He_n quasimolecular complexes[22] whose absorption bands do not overlap with the wavelength of our excitation laser.

V. CONCLUSION

In summary, we have investigated experimentally and theoretically the spectrum of the D_1 transition of Ba^+ ion solvated in superfluid ^{4}He. The trapping site structure is modeled by the atomic bubble model using two different sets of *ab initio* pair potentials available in the literature. The results of the calculations are compared with the experimental data. It is found that the enhancement of the He density around the ion due to the electrostriction has a relatively small effect on the spectrum of the electronic transition. The atomic bubble model that does not take into account this density enhancement, still provides the results in a qualitative agreement with the experiment. The ion injection into superfluid He is achieved by crossing a gas-liquid interface in a large static electric field. The details of this process presently are not fully understood and require further study.

ACKNOWLEDGMENTS

We would like to thank P. Leiderer, Y. Lysogorskii and Y. Matsuo for fruitful discussions and suggestions. We would like to thank Y. Moriwaki, T. G. Wright, M. Mella and F. Cargnoni for sending us the calculated pair-potentials. We would like to thank M. Watanabe and P. Blumhardt for their help in the experimental set up construction. This work was partially supported by JSPS KAKENHI Grant number 24000007. This work was partially funded by the subsidy allocated to Kazan Federal University for the state assignment in the sphere of scientific activities (No. 3.8138.2017/8.9).

[1] W. W. Johnson and W. I. Glaberson, Phys. Rev. Lett. **29**, 214 (1972).
[2] H. Reyher, H. Bauer, C. Huber, R. Mayer, A. Schafer, and A. Winnacker, Phys. Lett. A **115**, 288 (1986).
[3] W. I. Glaberson and W. W. Johnson, J. Low Temp. Phys. **20**, 313 (1975).
[4] M. Cole and R. A. Bachman, Phys. Rev. B **15**, 1388 (1977).
[5] H. Bauer, M. Beau, B. Friedl, C. Marchand, K. Miltner, and H. Reyher, Phys. Lett. A **146**, 134 (1990).
[6] S. L. Fiedler, D. Mateo, T. Aleksanyan, and J. Eloranta, Phys. Rev. B **86**, 144522 (2012).
[7] D. Mateo, A. Leal, A. Hernando, M. Barranco, M. Pi, F. Cargnoni, M. Mella, X. Zhang, and M. Drabbels, J. Chem. Phys. **140**, 131101 (2014).
[8] P. Moroshkin, A. Hofer, and A. Weis, Phys. Rep. **469**, 1 (2008).
[9] K. R. Atkins, Phys. Rev. **116**, 1339 (1959).
[10] L. An der Lan, P. Bartl, C. Leidlmair, R. Jochum, S. Denifl, O. Echt, and P. Scheier, Chem. Eur. J. **18**, 4411 (2012).
[11] S. Müller, M. Mudrich, and F. Stienkemeier, J. Chem. Phys. **131**, 044319 (2009).
[12] W. W. Johnson and W. I. Glaberson, Phys. Rev. A **10**, 868 (1974).
[13] M. Foerste, H. Günther, O. Riediger, J. Wiebe, and G. zu Putlitz, Z. Phys. B **104**, 317 (1997).
[14] J. P. Toennies and A. F. Vilesov, Angew. Chem. Int. Ed. **43**, 2622 (2004).
[15] X. Zhang and M. Drabbels, J. Chem. Phys. **137**, 051102 (2012).
[16] A. Leal, X. Zhang, M. Barranco, F. Cargnoni, A. Hernando, D. Mateo, M. Mella, M. Drabbels, and M. Pi, J. Chem. Phys. **144**, 094302 (2016).
[17] R. Batulin, P. Moroshkin, D. Tayurskii, P. Blumhardt, P. Leiderer, and K. Kono, J. Low Temp. Phys. **175**, 63 (2014).
[18] S. Y. Ch'en and P. K. Henry, J. Quant. Spectrosc. Radiat. Transfer **13**, 385 (1973).
[19] G. L. Hammond, Astrophys. J. **136**, 431 (1962).
[20] Y. Fukuyama, Y. Moriwaki, and Y. Matsuo, PRA **69**, 042505 (2004).
[21] Y. Fukuyama, Y. Moriwaki, and Y. Matsuo, Phys. Rev. A **75**, 032725 (2007).

[22] P. Moroshkin and K. Kono, Phys. Rev. A **93**, 052510 (2016).
[23] Y. Moriwaki, [Private communication] (2013).
[24] Y. Moriwaki and N. Morita, Eur. Phys. J. D **13**, 11 (2001).
[25] M. F. McGuirk, L. A. Viehland, E. P. F. Lee, W. H. Breckenridge, C. D. Withers, A. M. Gardner, R. J. Plowright, and T. G. Wright, J. Chem. Phys. **130**, 194305 (2009).
[26] M. Mella and F. Cargnoni, J. Phys. Chem. A **118**, 6473 (2014).
[27] J. S. Cohen and B. Schneider, J. Chem. Phys. **61**, 3230 (1974).
[28] A. Kramida, Yu. Ralchenko, J. Reader, and NIST ASD Team, NIST Atomic Spectra Database (ver. 5.1), [Online]. Available: http://physics.nist.gov/asd [2014, July 16]. National Institute of Standards and Technology, Gaithersburg, MD. (2013).
[29] E. Condon and G. Shortley, Cambridge 460 (1959).
[30] A. Hickman, W. Steets, and N. Lane, Phys. Rev. B **12**, 3705 (1975).
[31] B. Tabbert, H. Günther, and G. zu Putlitz, J. Low Temp. Phys. **109**, 653 (1997).
[32] K. R. Atkins and Y. Narahara, Phys. Rev. A **138**, 437 (1985).
[33] R. L. Rusby, J. Low Temp. Phys. **58**, 203 (1985).
[34] E. C. Kerr, J. Chem. Phys. **26**, 511 (1957).
[35] T. Kinoshita, K. Fukuda, and T. Yabuzaki, Phys. Rev. B **54**, 6600 (1996).
[36] E. H. Pinnington, R. W. Berends, and M. Lumsden, J. Phys. B: At. Mol. Opt. Phys. **28**, 2095 (1995).
[37] Q. Hui, J. L. Persson, J. H. M. Beijersbergen, and M. Takami, Z. Phys. B **98**, 353 (1995).
[38] P. Moroshkin, V. Lebedev, and A. Weis, Europhys. Lett. **96**, 26002 (2011).
[39] S. Kanorsky, M. Arndt, R. Dziewior, A. Weis, and T. Hänsch, Phys. Rev. B **50**, 6296 (1995).
[40] H. Bauer, M. Beau, A. Bernardt, B. Friedl, and H. Reyher, Phys. Lett. A **137**, 217 (1989).
[41] B. Tabbert, M. Beau, H. Günther, W. Haubetaler, C. Hönninger, K. Meyer, B. Plagemann, and G. zu Putlitz, Z. Phys. B **97**, 425 (1995).
[42] I. Baumann, M. Foerste, K. Layer, G. zu Putlitz, B. Tabbert, and C. Zühlke, J. Low Temp. Phys. **110**, 213 (1998).
[43] A. Fujisaki, K. Sano, T. Kinoshita, Y. Takahashi, and T. Yabuzaki, Phys. Rev. Lett. **93**, 1039 (1997).
[44] J. H. M. Beijersbergen, Q. Hui, and M. Takami, Phys. Lett. A **181**, 393 (1993).
[45] P. Moroshkin, V. Lebedev, and A. Weis, Phys. Rev. A **87**, 022513 (2013).
[46] A. P. Volodin, M. S. Khaikin, and V. S. Edel'man, JETP Letters **26**, 543 (1977).
[47] P. Leiderer, W. Ebner, and V. B. Shikin, Surf. Sci. **113**, 405 (1982).
[48] V. B. Shikin, Physics Uspekhi **54**, 1203 (2011).
[49] V. Vadakkumbatt, E. Joseph, A. Pal, and A. Ghosh, Nature Commun. **5**, 4571 (2014).
[50] P. Moroshkin, P. Leiderer, and K. Kono, Phys. Fluids **29**, 047106 (2017).
[51] V. Lebedev, P. Moroshkin, and A. Weis, Phys. Rev. A **84**, 022502 (2011).
[52] P. Moroshkin, R. Batulin, P. Leiderer, and K. Kono, Phys. Chem. Chem. Phys. **18**, 26444 (2016).